SCIENCE CHINA
Chemistry

•ARTICLES•

January 2021 Vol.64 No.1: 109–115
https://doi.org/10.1007/s11426-020-9881-7

Encapsulation of ultrafine Pd nanoparticles within the shallow layers of UiO-67 for highly efficient hydrogenation reactions

Zhiming Cui[1], Ting Fan[1], Liyu Chen[1], Ruiqi Fang[1*], Chuanmao Li[1,2] & Yingwei Li[1*]

[1]*State Key Laboratory of Pulp and Paper Engineering, School of Chemistry and Chemical Engineering, South China University of Technology, Guangzhou 510640, China;*
[2]*Guangzhou Keneng Cosmetics Scientific Research Co., Ltd., Guangzhou 510800, China*

Received July 16, 2020; accepted September 27, 2020; published online October 10, 2020

Metal-organic frameworks (MOFs) have been used to encapsulate active metal nanoparticles (MNPs) to fabricate MNPs@MOFs composites with high catalytic efficiencies. However, the diffusion of reactants and the accessibility of MNPs located in the center of MOFs may be hindered due to the inherent microporous structures of MOFs, which would affect the catalytic activities of MNPs. Herein, we report a solvent assisted ligand exchange-hydrogen reduction (SALE-HR) strategy to selectively encapsulate ultrafine MNPs (Pd or Pt) within the shallow layers of a MOF, i.e., UiO-67. The particle sizes of the encapsulated MNPs and the thickness of the MNPs-embedded layers can be adjusted easily by controlling the SALE conditions (*e.g.* time and temperature). Crucially, the LE-Pd@UiO-80-0.5 composite with the thinnest Pd-embedded layers displays remarkable catalytic efficiency with a high turnover frequency (TOF) value of 600 h^{-1} towards hydrogenation of nitrobenzene under 1 atm H_2 at room temperature. The results indicate that the catalytic efficiency and the utilization of MNPs can be enhanced by compactly encapsulating MNPs within the shallow layers of MOFs as close to their outer surfaces as possible, owing to the short mass-transfer distance and enhanced accessibility of overall MNPs.

Metal-organic frameworks, metal nanoparticles, heterogeneous catalysis, encapsulation, hydrogenation

Citation: Cui Z, Fan T, Chen L, Fang R, Li C, Li Y. Encapsulation of ultrafine Pd nanoparticles within the shallow layers of UiO-67 for highly efficient hydrogenation reactions. *Sci China Chem*, 2021, 64: 109–115, https://doi.org/10.1007/s11426-020-9881-7

1 Introduction

Metal-based catalysts have shown considerable performances in heterogeneous catalysis for the production of various valuable products. With the development of modern chemical industry, enormous efforts have been devoted to the design and fabrication of highly efficient metal-based heterogeneous catalysts [1–7]. As a result, a series of synthesis strategies have been developed, including coprecipitation [8], sol-gel [9], electro-deposition [10], and impregnation-reduction methods [11]. Among the various synthesis strategies [12–17], metal encapsulation, *i.e.*, to uniformly disperse the nanoscale guest molecules within the pores/layers/vacancies of the porous supports [18–22], has been considered as one of the most effective protocols to enrich the amounts of active sites and enhance the interactions between the guest molecules and supports, thus promoting the activity and durability of the as-prepared catalysts through nano-confinement and size effects [23–25].

Porous materials (PM), including metal-organic frameworks (MOFs), zeolites and silicates, have been widely utilized for the encapsulation of metal species (MSs) like nanoparticles (NPs), clusters and even single atoms for the preparation of MS@PM composites [26–28]. In particular, MOFs, which feature with high specific areas and tunable nanoarchitectures, have drawn intense research attentions for the encapsulation of MSs within their layers, channels and pores [24,25,29,30]. For example, Xu *et al*. [31] reported a

*Corresponding authors (email: liyw@scut.edu.cn; fangrq@scut.edu.cn)

sequential double-solvent approach and liquid-phase concentration-controlled reduction strategy for the immobilization of AuNi alloy within the pores of MIL-101. The as-prepared AuNi@MIL-101 possessed homogeneous distribution of AuNi alloys in ultrasmall sizes and achieved a remarkable performance in the hydrolytic dehydrogenation of NH_3BH_3 at room temperature. Behm *et al*. [32] prepared a Cu/UiO-66 through anchoring Cu single atoms onto the –OH/–OH_2 groups of UiO-66. Benefitting from the atomically dispersed and positively charged Cu species, the obtained Cu/UiO-66 composite exhibited significantly high catalytic activity in CO oxidization. Su *et al*. [33] introduced Pt nanorods into the 1D channel of Pd-PCN-222(Hf), which showed unprecedented catalytic performances in the photocatalytic hydrogen evolution reaction.

More recently, a newly invented solvent assisted ligand exchange (SALE) approach was reported for the introduction of different MSs into the pores of MOFs. The morphology, composition and porosity of the obtained MOF-based composites could be precisely modified through tuning the pre-synthesized composites, MOF templates and SALE conditions [34,35]. Pan *et al*. [36] prepared Ru/Rh-coordinated complexes such as [Ru(Cy*)(bpydc)Cl]Cl·H_2O or [Rh(Cp*)-(bpydc)Cl]Cl·H_2O for the introduction of single-site Ru/Rh into the pores of UiO-67 through SALE. Tsung *et al*. [37] demonstrated the introduction of Ru complexes ($^{t\mathrm{Bu}}$PNP)Ru-(CO)-HCl, whose size was larger than that of the UiO-66 apertures, into the pores of UiO-66 through SALE. In spite of the advances made, the bottleneck of SALE was its inefficient regulation towards the spatial distribution of MSs, and therefore generally resulted in the homogeneous dispersion of MSs within the frameworks of MOFs. In terms of heterogeneous catalysis, the micrometer-scaled bulk crystallites of MOFs featuring microporous structures would hinder the mass transfer process of reactants and limit the accessibility of MSs distributing within the inner layers, consequently lowering the availability of MSs and the catalytic efficiency [38,39]. Therefore, in terms of the pursuit for advanced catalytic performances, it is highly desired to develop an efficient synthesis strategy to selectively encapsulate MSs within the shallow layers as close to the outer surface of MOFs as possible.

This work demonstrates the fabrication of a series of LE-M@UiO-*T*-*t* composites (where LE represents ligand-exchanged, M represents the encapsulated MS including Pd or Pt NP, *T* and *t* are the temperature (°C) and time (h) of the SALE process, respectively) with unique core@shell nanostructures with MSs selectively encapsulated within the shell through the SALE method. Noteworthy, the composition of the composites as well as the location and sizes of the encapsulated MSs could be easily modified by tuning the time and temperature of SALE. Subsequently, the obtained LE-Pd@UiO-80-*t* composites are employed as the catalysts in nitrobenzene hydrogenation [21,22,40,41], which, as expected, exhibit remarkably enhanced catalytic performances compared with noble metals@microporous supports prepared by the conventional methods under the same reaction conditions. Among the investigated composites, the LE-Pd@UiO-80-0.5 shows the highest catalytic efficiency, achieving an almost quantitative conversion from nitrobenzene to aniline under 1 atm H_2 at room temperature, with a turnover frequency (TOF) value as high as 600 h^{-1}.

2 Results and discussion

In order to prove the thermodynamic accessibility of the SALE process between the original ligand of UiO-67 (*i*. *e*., 4,4'-biphenyldicarboxylic acid, H_2bpdc) and introduced ligand H_2bpydc-$PdCl_2$, density functional theory calculation (DFT) was conducted before the experiments. The model used to compute ligand exchange is shown in Figure S1. The DFT results pointed out a negative solvated free energy of the reaction (ΔG=−1.73 kcal/mol), indicating that the assembling between H_2bpydc-$PdCl_2$ and the Zr^{4+} nodes of UiO-67 was thermodynamically favorable.

Supported by the DFT results, H_2bpydc-$PdCl_2$ was prepared as the introduced ligand for the subsequent SALE process. X-ray photoelectron spectroscopy (XPS) and ^{1}H nuclear magnetic resonance (^{1}H NMR) experiments were conducted to verify the chelation between H_2bpydc and Pd^{2+}. In the XPS spectra of H_2bpydc-$PdCl_2$, two peaks were observed at 337.6 and 342.9 eV (Figure S2a), which were assigned to divalent Pd. Besides, the binding energy of N 1s peak of the ligands shifted to a higher value by about 1.0 eV as compared with the pristine H_2bpydc (Figure S2b), which was related to the partial electron transfer from pyridine N to Pd^{2+}, verifying the successful chelation between H_2bpydc and Pd^{2+} [42]. Similarly, in comparison with pristine H_2bpydc, the ^{1}H NMR peaks of the ortho- and para-protons of pyridine N on the as-prepared H_2bpydc-$PdCl_2$ were obviously shifted towards the low field, while the meta-proton of pyridine N on the Pd-embracing ligands shifted towards the high field (Figure S3). These shifts could be ascribed to the electron-withdrawing conjugation effect caused by Pd^{2+}, further confirming the chelation interaction between H_2bpydc and Pd^{2+} [43].

The typical synthesis route of LE-M@UiO-*T*-*t* is illustrated in Scheme 1. Taking the synthesis of LE-Pd@UiO-80-0.5 as an example, UiO-67 was primarily synthesized under solvothermal condition according to the reported procedure with some modifications [44]. Afterwards, 2,2'-bipyridine-5,5'-dicarboxylic acid ligands (H_2bpydc) were served as the anchoring ligands for Pd^{2+} to prepare the metalloligands (H_2bpydc-$PdCl_2$). Subsequently, H_2bpydc-$PdCl_2$ was used to substitute for the initial ligand (i.e., H_2bpdc) at

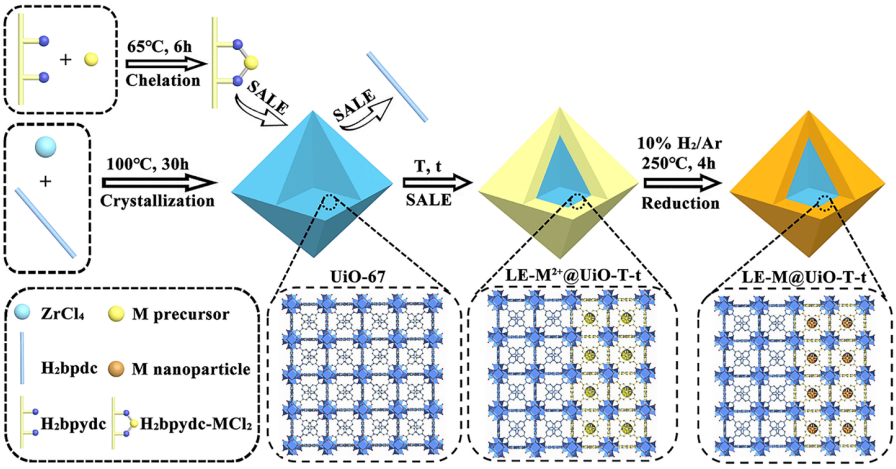

Scheme 1 Synthesis routes of LE-M@UiO-*T*-*t* via SALE-HR strategy (color online).

the shallow layers of UiO-67 through the SALE method at 80°C for 0.5 h, followed by hydrogen reduction (HR) of the Pd in 10% H_2/Ar at 250°C.

X-ray diffraction (XRD) was conducted to examine the structure of the LE-Pd@UiO-80-0.5 composite. Strong characteristic diffraction peaks of UiO-67 were observed at 5.7° and 6.6° in the XRD patterns of LE-Pd@UiO-80-0.5 (Figure 1(a)), indicating that the phase integrity and crystallinity of UiO-67 were well preserved after the SALE-HR process. In the N_2-sorption experiments, the LE-Pd@UiO-80-0.5 composite showed a typical type I sorption isotherm and narrow pore size distribution (<2 nm), revealing its microporous regime inheriting from the parent UiO-67 (Figure 1(b, c)). It is noteworthy that the Brunauer-Emmett-Teller (BET) specific surface area (1,235 m^2/g) and pore volume (0.65 cm^3/g) of the LE-Pd@UiO-80-0.5 were remarkably reduced in comparison with the pristine UiO-67, indicating that partial cavities in the shallow layers of UiO-67 were occupied by Pd NPs (Figure 1(b, c) and Table S1). XPS analysis was further conducted to interpret the valence states of Pd and N. The survey XPS spectra of LE-Pd@UiO-80-0.5 verified the co-existence of Zr, Pd, C, N and O elements (Figure 1(d)). In the high-resolution spectra, the peaks at 335.4 eV (Pd $3d_{5/2}$) and 341.3 eV (Pd $3d_{3/2}$), along with the presence of their characteristic shake-up satellite peaks, suggested the presence of metallic Pd^0 species in LE-Pd@UiO-80-0.5 (Figure 1(e)) [45]. Meanwhile, the characteristic peak at 399.3 eV in N 1s region was assigned to pyridine N, pointing out that the H_2bpydc ligands were successfully incorporated onto the Zr^{4+} nodes to fabricate the LE-Pd@UiO-80-0.5 (Figure 1(f)) [45].

Scanning electron microscopy (SEM) and transmission electron microscopy (TEM) were used to characterize the morphology and structure of the as-prepared samples. The parent UiO-67 exhibited the mono-dispersed octahedral crystalline with a size of *ca.* 1.2 μm and smooth external surfaces (Figure S4). After the SALE process at 80°C for 0.5 h and hydrogen reduction, the octahedral morphology and crystal structure of LE-Pd@UiO-80-0.5 were well preserved (Figure 2(a)). The high-resolution TEM (HR-TEM) images and particle size distribution results revealed that the Pd NPs were in ultrafine sizes of *ca.* 1.85 nm with the interplanar spacing of 0.224 nm, in accordance with the spacing of the (111) planes of face-centered cubic (fcc) Pd^0

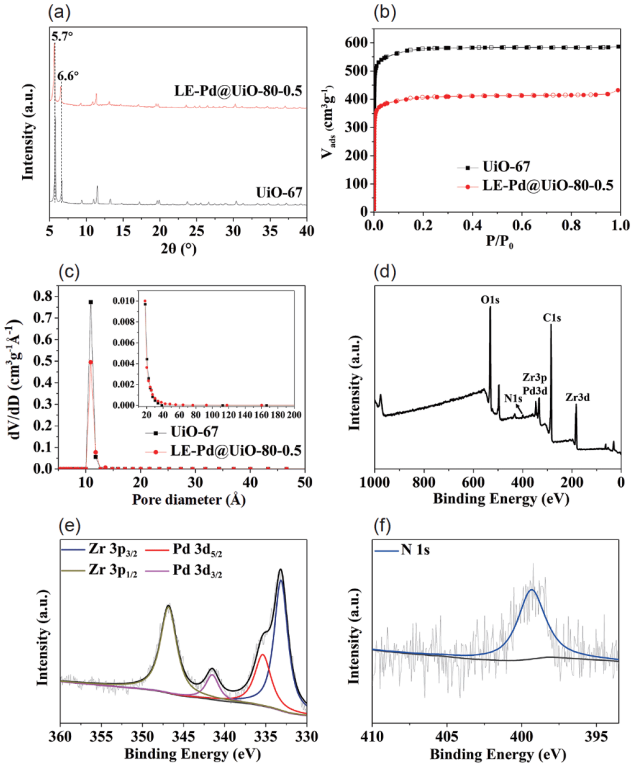

Figure 1 (a) XRD patterns, (b) N_2 adsorption/desorption isotherms and (c) pore size distributions of UiO-67 and LE-Pd@UiO-80-0.5; (d) full scan, (e) Pd 3d and (f) N 1s regions of the XPS spectra of LE-Pd@UiO-80-0.5 (color online).

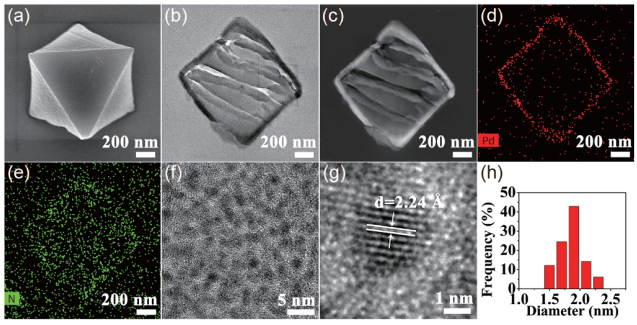

Figure 2 (a) SEM image of LE-Pd@UiO-80-0.5; (b) TEM image, (c) STEM image, (d) Pd elemental mapping, (e) N elemental mapping, (f, g) HR-TEM images and (h) Pd particle size distributions of LE-Pd@UiO-80-0.5 ultrathin cuts (color online).

(Figure 2(f–h)) [45]. Particularly, TEM, high-angle annular dark-field scanning transmission electron microscopy (HAADF-STEM) and corresponding Pd and N elemental mapping experiments were carried out on the ultrathin cuts of the LE-Pd@UiO-80-0.5 composite to further explore the distribution of Pd NPs inside the bulk crystals. And the results suggested that the ultrafine Pd NPs were homogeneously distributed throughout the shallow layers of the LE-Pd@UiO-80-0.5 bulks in depth of *ca.* 56 nm (Figure 2 (b–d)), while the H_2bpydc ligands were introduced into the shallow layers of the LE-Pd@UiO-80-0.5 according to the N elemental mapping (Figure 2(e), noting that the N elemental mapping was affected by the resin used for embedding the sample). Besides, the Pd content of LE-Pd@UiO-80-0.5 was about 0.3 wt% as measured by atomic absorption spectroscopy (AAS), in good agreement with the inductively-coupled plasma optical emission spectrometry (ICP-OES) results.

Furthermore, ^{1}H NMR was conducted to quantify the ligand ratios of the as-prepared LE-Pd@UiO-80-*t* samples. As shown in the ^{1}H NMR spectra (Figure S9(a–c)), the peaks at about 7.65 ppm (d, *J*=8 Hz, 4H) and 7.85 ppm (d, *J*=8 Hz, 4H) were assigned to the protons of H_2bpdc ligands, while the peaks at about 8.60 ppm (s, 2H), 8.40 ppm (d, *J*=8 Hz, 2H) and 8.10 ppm (d, *J*=8 Hz, 2H) were assigned to the protons of H_2bpydc ligands, suggesting that the H_2bpydc ligands were successfully incorporated onto the Zr^{4+} nodes to fabricate the LE-Pd@UiO-80-*t* composites. Significantly, the molar ratios of H_2bpydc ligands in LE-Pd@UiO-80-0.5, LE-Pd@UiO-80-1 and LE-Pd@UiO-80-2 were calculated to be 9%, 15.3% and 21.1%, respectively. The ^{1}H NMR results were in good agreement with the Pd and N contents measured by AAS and element analysis (EA), respectively (Table 1), suggesting a prolonged time was beneficial to introduce more H_2bpydc ligands into the samples via the ligand exchanging process.

On the other hand, to explore the impact of the SALE temperatures on their structural properties, LE-Pd@UiO-*T*-1 (*T* = 40, 60 and 100°C) composites were prepared at different SALE temperatures. SEM images showed that the octahedral morphology of LE-Pd@UiO-*T*-1 was preserved after the SALE-HR process (Figure 3(a1–d1)), in agreement with the XRD diffraction results (Figure S7). However, increasing the temperature from 40°C to 100°C led to rougher external surfaces on the obtained composites. TEM images revealed that an increase in temperature could also result in an enhancement in the thicknesses of the Pd-containing shallow layers, which were 48, 78 and 129 nm for LE-Pd@UiO-40-1, LE-Pd@UiO-60-1 and LE-Pd@UiO-80-1, respectively. These results indicated that the Pd-containing shallow layers could also be modified by varying the SALE temperature (Figure 3).

The SALE temperatures can also influence the size of the Pd NPs. When the SALE treatment was carried out at 40°C, the size of the obtained Pd NPs was 2.15 nm (Figure 3(a6, a7)). When the SALE temperature was raised, the average size of Pd NPs was gradually decreased to 2.07 at 60°C and 1.85 nm at 80°C, respectively (Figure 3(b6, b7) and (c6, c7)). However, a further increase of the temperature to 100°C led to remarkably enhanced Pd NP sizes to *ca.* 2.43 nm (Figure 3 (d6, d7)). Besides, ^{1}H NMR confirmed the incorporation of H_2bpydc ligands in the as-prepared LE-Pd@UiO-*T*-1 (Figure S9b, d–f). An increased ligand exchanging temperature from 40 to 100°C resulted in higher H_2bpydc ligand contents from 7.5% to 19.6%. The ^{1}H NMR results were also in good agreement with the Pd and N contents obtained by AAS and elemental analysis (Table 1), suggesting a higher temperature was favorable for enhanced Pd contents because more H_2bpydc-$PdCl_2$ ligands could be coordinated onto the Zr^{4+}

Table 1 Thickness of Pd-embedded layers, ligand exchange ratio and elemental contents of the as-prepared composites

Sample	Thickness of Pd-embedded layers (nm)	Ligand exchange ratio (%)	Elemental content (wt%)		
			C	N	Pd
LE-Pd@UiO-80-0.5	56	9.0	41.8	1.0	0.3
LE-Pd@UiO-80-1	129	15.3	40.6	1.1	1.0
LE-Pd@UiO-80-2	193	21.1	42.0	1.4	1.6
LE-Pd@UiO-40-1	48	7.5	41.9	0.6	0.3
LE-Pd@UiO-60-1	78	10.9	41.7	0.8	0.5
LE-Pd@UiO-100-1	127	19.6	40.8	1.6	1.1

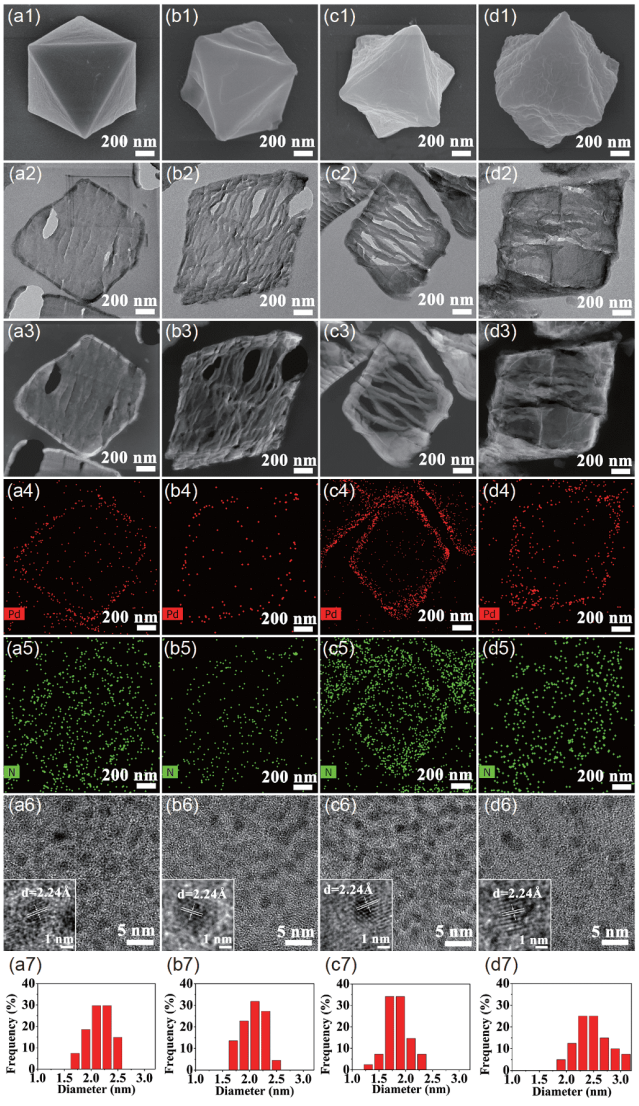

Figure 3 (a1–d1) SEM images of (a) LE-Pd@UiO-40-1, (b) LE-Pd@UiO-60-1, (c) LE-Pd@UiO-80-1 and (d) LE-Pd@UiO-100-1; (a2–d2) TEM, (a3–d3) STEM, (a4–d4) Pd mapping, (a5–d5) N mapping, (a6–d6) HR-TEM images and (a7–d7) Pd particle size distributions of (a) LE-Pd@UiO-40-1, (b) LE-Pd@UiO-60-1, (c) LE-Pd@UiO-80-1 and (d) LE-Pd@UiO-100-1 ultrathin cuts (color online).

nodes via ligand exchanges. Some control experiments were further conducted to exclude the physical adsorption of H_2bpydc-$PdCl_2$ ligands on UiO-67. The Me-Pd/UiO was prepared under the same conditions as LE-Pd@UiO-80-0.5 except using Me_2bpy-$PdCl_2$ (pre-synthesized by the coordination of 5,5'-dimethyl-2,2'-bipyridine (Me_2bpy) and $PdCl_2$) as the introduced ligand. No characteristic peaks of Me_2bpy were observed in the ^{1}H NMR spectra of Me-Pd/UiO (Figure S10), and the Pd content was below the detecting limits of AAS, indicating that the free Me_2bpy-$PdCl_2$ compounds were removed by washing. Therefore, we could infer that the H_2bpydc-$PdCl_2$ ligands were exclusively coordinated onto the Zr^{4+} nodes of UiO-67 to fabricate the Pd-containing shallow layers. Finally, the introduced Pd species were completely reduced by H_2 and encapsulated within the shallow layers of the composites according to the XPS and TEM characterizations (Figure S11; Figure S5 and Figure 3).

Based on the characterization results, we assumed that the sizes of Pd NPs were simultaneously affected by the rates of mass-transfer and coordination process [46,47]. During the SALE treatment, the UiO-67 templates underwent a dissolution and self-assembling process, in which the dissolution of original ligands (H_2bpdc) and the coordination of introduced ligands (H_2bpydc-$PdCl_2$) were simultaneously occurred. At low temperatures (*e. g.* 40°C), the inverse concentration gradient mass-transfer rate of H_2bpydc-$PdCl_2$ was much inferior to its self-assembling rate, and hence the ligand exchanging mostly occurred at the shallow layers, leading to big sizes of Pd NPs. Raising the temperature led to a higher mass-transfer rate and consequently a decreased density of H_2bpydc-$PdCl_2$ at the shallow layers, resulting in reduced particle sizes. However, the enlarged sizes of Pd NPs in LE-Pd@UiO-100-1 may be attributed to the partial decomposition of UiO-67 and unwilling slight aggregations of H_2bpydc-$PdCl_2$ species [48]. In addition, the BET specific surface areas and pore volumes of the composites displayed a negatively-correlated trend with the rising temperatures, which was possibly ascribed to the increasing Pd loadings and crystalline disorders resulting from the dissolution and self-assembling process (Figure S8 and Table S1).

Our strategy was also applicable to the encapsulation of Pt NPs within the UiO-67 pores. Typically, H_2bpydc-$PtCl_2$ was pre-synthesized and employed as the precursor in the subsequent SALE-HR process at 80°C for 1 h. The obtained LE-Pt@UiO-80-1 featured mono-dispersed octahedral crystalline with well-preserved integrity in sizes of *ca.* 1.1 μm with rough surfaces (Figure S12a and Figure S13a). TEM and HR-TEM images on the ultrathin cuts of the composite indicated the successful confinement of ultrasmall Pt NPs (1.6±0.4 nm) in the shallow layer in a depth of 143 nm (Figure S12b–h). The lattice fringe of Pt NPs was about 0.226 nm, corresponding to the spacing of the (111) planes of face-centered cubic (fcc) Pt [49]. The N_2 adsorption/desorption results proved the porosity of LE-Pt@UiO-80-1, whose S_{BET}, $S_{Langmuir}$ and pore volume were 1,225 m^2/g, 1,778 m^2/g and 0.63 cm^3/g, respectively (Figure S13b–c). Besides, the Pt $4f_{7/2}$ and Pt $4f_{5/2}$ peaks in XPS spectra were located at 71.4 eV and 74.6 eV, respectively, implying that the Pt species were completely reduced to metallic Pt NPs (Figure S13e) with a mass fraction of ca. 1.1 wt% (determined by AAS) [50]. Meanwhile, the characteristic peak of pyridine N in N 1s region was located at 399.4 eV, suggesting the bpydc ligands were successfully introduced onto the Zr^{4+} nodes to fabricate the LE-Pt@UiO-80-1 composite (Figure S13f).

Subsequently, the as-obtained LE-Pd@UiO-80-*t* composites were employed as catalysts for the hydrogenation of

nitrobenzene (NB) to aniline (AN). All the hydrogenation reactions were carried out under atmospheric pressure of H_2 at room temperature in methanol solution. For comparison, the Pd-in-UiO and Pd/UiO counterparts were also prepared [21,51] (Figure S14 and S15) and employed in this reaction. The catalytic performances of the as-prepared materials were summarized in Figure 4. In the blank experiment, the NB conversion over the pristine UiO-67 was below the detection limit of gas chromatography-mass spectrometry (GC-MS), revealing the essential role of Pd NPs as active sites for this reaction. As expected, all of the LE-Pd@UiO-80-*t* composites showed remarkable catalytic efficiencies in the reaction, achieving nearly quantitative yields of AN under 1 atm H_2 at room temperature (Figure 4(a)). In particular, the depth of the Pd-containing shallow layers had a significant impact on the catalytic performances. The catalytic reactivity was inversely proportional to the depth of Pd-containing shallow layers (Figure 4(b)). The LE-Pd@UiO-80-0.5 with a 56 nm shallow layer attained a TOF value as high as 600 h^{-1}, outperforming the other investigated materials. Therefore, we could conclude that the catalytic efficiency and the accessibility of Pd NPs could be promoted by selectively confining the Pd NPs within MOF pores as close to the external surface as possible to shorten the mass-transfer distance and promote the accessibility of the Pd NPs. In addition, the LE-Pd@UiO-80-*t* composites exhibited remarkably enhanced catalytic performances in comparison with Pd/UiO, which may be attributed to the ultrafine sizes of Pd NPs and the presence of pyridine N within the pores. In addition, in comparison with noble-metal-based encapsulated catalysts synthesized by the conventional methods, the LE-Pd@UiO-80-0.5 reported in this work showed higher or comparable catalytic performance under relatively mild reaction conditions, demonstrating the advantage of the SALE-HR strategy proposed in this work (Table S2).

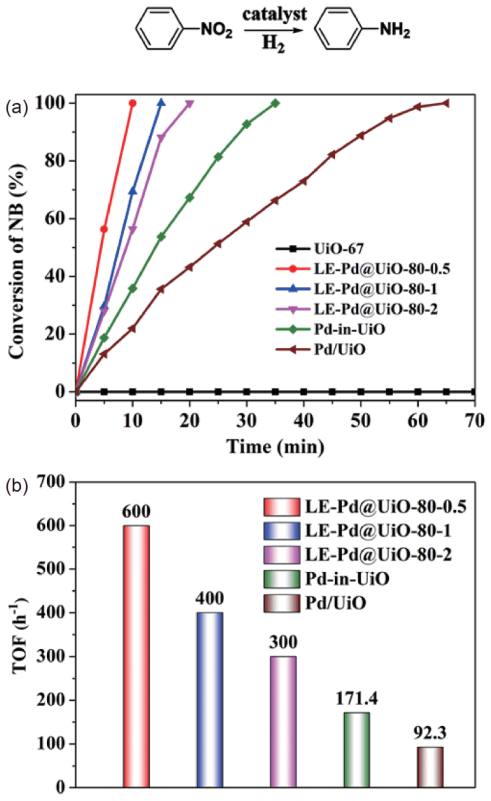

Figure 4 (a) Catalytic kinetic curves and (b) comparison of TOF values of the materials. Reaction conditions: nitrobenzene (0.1 mmol), catalysts (1 mol% Pd, determined by ICP-OES), methanol (2 mL) and 1 atm H_2, room temperature (color online).

In practical applications, the stability and durability of catalysts are of vital importance. After reaction, the LE-Pd@UiO-80-0.5 catalyst was separated by centrifugation, thoroughly washed by methanol, dried under vacuum and then directly reused under identical conditions (Figure S16a). To our delight, in the fifth cycle, the NB was almost quantitatively converted into AN in 10 min with a TOF value of 600 h^{-1}. No significant activity or selectivity loss was observed (Figure S16b), indicating its good recyclability. Besides, the sizes of the Pd NPs in the spent LE-Pd@UiO-80-0.5 were also well retained (Figure S16c–e) with a Pd content of 0.3 wt% (determined by ICP-OES), suggesting the reliable stability of the catalyst, which may be ascribed to the confinement effect of the UiO-67 frameworks (Figure S16f–g).

Finally, a series of substituted nitroarenes were employed as substrates to examine the substrate tolerance of LE-Pd@UiO-80-0.5. As summarized in Table S3, all the investigated nitroarenes were selectively transformed into the corresponding anilines, demonstrating the good tolerance of LE-Pd@UiO-80-0.5 towards different nitroarenes.

3 Conclusions

In summary, we have developed a novel SALE-HR strategy to encapsulate ultrafine Pd NPs within the shallow layers of UiO-67. The synthesis is facile and simple, only involving the pre-synthesis of UiO-67, subsequent ligand exchanging and final reduction. The as-prepared LE-Pd@UiO-*T*-*t* composites featured mono-dispersed octahedral crystalline and evenly distributed ultrafine Pd NPs in the shallow layers of UiO-67. It is noteworthy that the sizes of Pd NPs and depth of shallow layers could be facilely tuned through adjusting the synthesis parameters of SALE (*e. g.* time and temperature). The LE-Pd@UiO-80-*t* materials exhibited remarkable catalytic performances in the hydrogenation of nitroarenes. Particularly, the LE-Pd@UiO-80-0.5 composite with the Pd-containing shallow layers in depth of 56 nm exhibited the highest catalytic efficiency among the as-prepared composites, achieving a nearly quantitative conversion of nitrobenzene to aniline with a TOF value as high as 600 h^{-1}. This work might open an avenue for the encapsulation of

nanoparticles, nanoclusters or even single atoms of various metals within porous materials like MOFs for frontier applications including heterogenous catalysis as demonstrated here.

Acknowledgements This work was supported by the National Natural Science Foundation of China (21825802, 21908068), the Fundamental Research Funds for the Central Universities (2019PY11, 2019MS041), the Science and Technology Program of Guangzhou (201804020009), the State Key Laboratory of Pulp and Paper Engineering (2017ZD04, 2018TS03), and the Natural Science Foundation of Guangdong Province (2016A050502004, 2017A030312005, 2020A1515010376).

Conflict of interest The authors declare no conflict of interest.

Supporting information The supporting information is available online at http://chem.scichina.com and http://link.springer.com/journal/11426. The supporting materials are published as submitted, without typesetting or editing. The responsibility for scientific accuracy and content remains entirely with the authors.

1 Ye R, Zhukhovitskiy AV, Deraedt CV, Toste FD, Somorjai GA. *Acc Chem Res*, 2017, 50: 1894–1901
2 Meemken F, Baiker A. *Chem Rev*, 2017, 117: 11522–11569
3 Shokouhimehr M, Hong K, Lee TH, Moon CW, Hong SP, Zhang K, Suh JM, Choi KS, Varma RS, Jang HW. *Green Chem*, 2018, 20: 3809–3817
4 Shokouhimehr M, Kim T, Jun SW, Shin K, Jang Y, Kim BH, Kim J, Hyeon T. *Appl Catal A-General*, 2014, 476: 133–139
5 Shokouhimehr M, Lee JE, Han SI, Hyeon T. *Chem Commun*, 2013, 49: 4779–4781
6 Cui J, Liu T, Zhang Q, Wang T, Hou X. *Chem Eng J*, 2021, 404: 126453
7 Das R, Sypu VS, Paumo HK, Bhaumik M, Maharaj V, Maity A. *Appl Catal B-Environ*, 2019, 244: 546–558
8 Jang MJ, Yang J, Lee J, Park YS, Jeong J, Park SM, Jeong JY, Yin Y, Seo MH, Choi SM, Lee KH. *J Mater Chem A*, 2020, 8: 4290–4299
9 Ma S, Zhao X, Li Y, Zhang T, Yuan F, Niu X, Zhu Y. *Appl Catal B-Environ*, 2019, 248: 226–238
10 Sriram P, Kumar MK, Selvi GT, Jha NS, Mohanapriya N, Jha SK. *Electrochim Acta*, 2019, 323: 134809
11 Ning L, Liao S, Liu X, Guo P, Zhang Z, Zhang H, Tong X. *J Catal*, 2018, 364: 1–13
12 Li J, Li K, Sun L, Zhang Z, Wu Z, Zhang Y, Yang X. *Sci China Chem*, 2020, 63: 519–525
13 Ling X, Xu Y, Wu S, Liu M, Yang P, Qiu C, Zhang G, Zhou H, Su C. *Sci China Chem*, 2020, 63: 386–392
14 Sun X, Wang P, Shao Z, Cao X, Hu P. *Sci China Chem*, 2019, 62: 1686–1697
15 Wang G, Luo R, Yang C, Song J, Xiong C, Tian H, Zhao ZJ, Mu R, Gong J. *Sci China Chem*, 2019, 62: 1710–1719
16 Luneau M, Shirman T, Foucher AC, Duanmu K, Verbart DMA, Sautet P, Stach EA, Aizenberg J, Madix RJ, Friend CM. *ACS Catal*, 2019, 10: 441–450
17 Zhang J, Wang H, Wang L, Ali S, Wang C, Wang L, Meng X, Li B, Su DS, Xiao FS. *J Am Chem Soc*, 2019, 141: 2975–2983
18 Bugaev AL, Guda AA, Lomachenko KA, Kamyshova EG, Soldatov MA, Kaur G, Øien-Ødegaard S, Braglia L, Lazzarini A, Manzoli M, Bordiga S, Olsbye U, Lillerud KP, Soldatov AV, Lamberti C. *Faraday Discuss*, 2018, 208: 287–306
19 Chen L, Chen H, Li Y. *Chem Commun*, 2014, 50: 14752–14755
20 Shen L, Wu W, Liang R, Lin R, Wu L. *Nanoscale*, 2013, 5: 9374–9382
21 Chen L, Chen H, Luque R, Li Y. *Chem Sci*, 2014, 5: 3708–3714
22 Chen L, Huang W, Wang X, Chen Z, Yang X, Luque R, Li Y. *Chem Commun*, 2017, 53: 1184–1187
23 Liang J, Liang Z, Zou R, Zhao Y. *Adv Mater*, 2017, 29: 1701139
24 Yang Q, Xu Q, Jiang HL. *Chem Soc Rev*, 2017, 46: 4774–4808
25 Li G, Zhao S, Zhang Y, Tang Z. *Adv Mater*, 2018, 30: 1800702
26 Fang R, Tian P, Yang X, Luque R, Li Y. *Chem Sci*, 2018, 9: 1854–1859
27 Qiu X, Chen J, Zou X, Fang R, Chen L, Chen Z, Shen K, Li Y. *Chem Sci*, 2018, 9: 8962–8968
28 Chen Y, Ji S, Chen C, Peng Q, Wang D, Li Y. *Joule*, 2018, 2: 1242–1264
29 Furukawa H, Cordova KE, O'Keeffe M, Yaghi OM. *Science*, 2013, 341: 1230444
30 Kirchon A, Feng L, Drake HF, Joseph EA, Zhou HC. *Chem Soc Rev*, 2018, 47: 8611–8638
31 Zhu QL, Li J, Xu Q. *J Am Chem Soc*, 2013, 135: 10210–10213
32 Abdel-Mageed AM, Rungtaweevoranit B, Parlinska-Wojtan M, Pei X, Yaghi OM, Behm RJ. *J Am Chem Soc*, 2019, 141: 5201–5210
33 Li S, Mei HM, Yao SL, Chen ZY, Lu YL, Zhang L, Su CY. *Chem Sci*, 2019, 10: 10577–10585
34 Deria P, Mondloch JE, Karagiaridi O, Bury W, Hupp JT, Farha OK. *Chem Soc Rev*, 2014, 43: 5896–5912
35 Karagiaridi O, Bury W, Mondloch JE, Hupp JT, Farha OK. *Angew Chem Int Ed*, 2014, 53: 4530–4540
36 Liao WM, Zhang JH, Wang Z, Yin SY, Pan M, Wang HP, Su CY. *J Mater Chem A*, 2018, 6: 11337–11345
37 Li Z, Rayder TM, Luo L, Byers JA, Tsung CK. *J Am Chem Soc*, 2018, 140: 8082–8085
38 Yang Q, Liu W, Wang B, Zhang W, Zeng X, Zhang C, Qin Y, Sun X, Wu T, Liu J, Huo F, Lu J. *Nat Commun*, 2017, 8: 14429
39 Wang B, Liu W, Zhang W, Liu J. *Nano Res*, 2017, 10: 3826–3835
40 Li J, Wu F, Lin L, Guo Y, Liu H, Zhang X. *Chem Eng J*, 2018, 333: 146–152
41 Sadeghzadeh SM, Zhiani R, Emrani S. *New J Chem*, 2018, 42: 988–994
42 Chen L, Gao Z, Li Y. *Catal Today*, 2015, 245: 122–128
43 Kelly NR, Goetz S, Hawes CS, Kruger PE. *Tetrahedron Lett*, 2011, 52: 995–998
44 Schaate A, Roy P, Godt A, Lippke J, Waltz F, Wiebcke M, Behrens P. *Chem Eur J*, 2011, 17: 6643–6651
45 Chen L, Chen X, Liu H, Bai C, Li Y. *J Mater Chem A*, 2015, 3: 15259–15264
46 Boissonnault JA, Wong-Foy AG, Matzger AJ. *J Am Chem Soc*, 2017, 139: 14841–14844
47 Jayachandrababu KC, Sholl DS, Nair S. *J Am Chem Soc*, 2017, 139: 5906–5915
48 Shao Z, Yu C, Xie Q, Wu Q, Zhao Y, Hou H. *Chem Commun*, 2019, 55: 13382–13385
49 Tian P, Shen K, Chen J, Fan T, Fang R, Li Y. *Small Methods*, 2018, 2: 1800219
50 Zhuang G, Bai J, Zhou X, Gao Y, Huang H, Cui H, Zhong X, Zhong CL, Wang J. *Eur J Inorg Chem*, 2017, 2017: 172–178
51 Fang R, Liu H, Luque R, Li Y. *Green Chem*, 2015, 17: 4183–4188